Journal of Applied Fluid Mechanics, Vol. 18, No. 12, pp. 2927-2940, 2025.
Available online at www.jafmonline.net, ISSN 1735-3572, EISSN 1735-3645.
https://doi.org/10.47176/jafm.18.12.3621

Numerical Investigation of Fluctuation Characters and Radial Force on Impeller within a Vortex Pump

Y. Wei[1†], H. Wei[2], Q. Fan[3] and X. Wang[1]

[1] *National Research Center of Pumps, Jiangsu University, Zhenjiang 212013, China*
[2] *Jiangsu Jingke Pump Co., Ltd., Taizhou 214537, China*
[3] *Zhejiang Fang Wei Testing Technology Co., Ltd., Hangzhou 311122, China*

† *Corresponding Author Email: wyy@ujs.edu.cn*

ABSTRACT

Owing to the unique operating mechanism of the vortex pump, which differs from that of conventional vane pumps, inherent high-frequency flow fluctuations occur within the pump, leading to the natural imposition of radial forces on the impeller. The present work conducted a study on a vortex pump by numerical simulation. The numerical results are validated by comparing with experimental data. Based on the numerical calculation results, the frequency domains of pressure pulsations at several typical locations are presented. The annular interface between the rotor and the stator is developed, the characteristics of pressure and velocity pulsations including their intensity as well as the distributions of time-averaged pressure and velocity components across this interface are presented. Finally, the transient characters of the radial force acting on the impeller is studied. The results show that the numerical calculation results are in good agreement with the experimental data. The helical flow at the impeller outlet exerts a pronounced influence on the inlet-proximal regions flanking the outlet on both sides of the impeller, resulting in relatively large pressure and velocity pulsations. The induced effect of the fluid helix leads to a relatively high flow velocity on the side close to the wall surface, causing the radial velocity at the middle part of the impeller outlet to be much greater than that at other positions.

Article History

Received April 30, 2025
Revised June 24, 2025
Accepted July 9, 2025
Available online October 6, 2025

Keywords:

Vortex pump
Pressure fluctuation
Velocity fluctuation
Radial force
Numerical simulation

1. INTRODUCTION

Vortex pumps, also referred to as a regenerative or peripheral pump, are widely utilized in handling fluids containing entrained gases, vapors, or suspended solids due to the non-clogging design of the flow path and the reduced mechanical shear within the vortex (Quan et al.2019a; Yang et al., 2025; Zhou et al., 2025a). The working principle relies on generating a helical vortex in the fluid, enabling energy transfer through repeated impeller-fluid interactions, leading to staged pressure buildup. Therefore, the impeller of a vortex pump is inherently subjected to unbalanced radial forces. Besides, the hydraulic efficiency is typically lower than that of centrifugal pumps, owing to energy losses from repeated fluid recirculation.

The internal flow dynamics-characterized by intense rotor-stator interactions, flow medium and vortices, exhibit more complex flow patterns, particularly under multiphase flow (Zhang et al., 2013; Imasaka et al., 2018; Ye et al., 2020; Zeng et al., 2024; Zhou et al., 2025a; He et al., 2023). To improving lifetime of peripheral pump impeller in cavitation flow, Mohsin and Yaqob (2022) conducted experiments to study the fluid flow in peripheral pump. The results shows that in cavitation flow, the surface-treated impeller with the lowest surface roughness exhibited an 84.86% reduction in mass loss. These findings confirm that precision surface finishing and advanced thermal spray coatings constitute highly effective strategies for enhancing cavitation erosion resistance of vortex pump impellers. Rogovyi et al. (2021) conducted optimal design of vortex pump for particle fluid flow to improve the wear characters. The findings shows that in addition to optimizing the impeller to enhance wear resistance, further optimization of the inlet and outlet pipelines is also critical for improving wear characteristics. This is because improving fluid inlet and outlet conditions can reduce flow separation from the pipe walls, which is essential for mitigating wear.

Due to the special structure of the vortex pump, its geometric dimensions, including impeller diameter, and blade number, have a significant impact on the internal flow. Therefore, a considerable amount of research effort has been devoted to optimizing the structural design of flow-through components (Červinka, 2012; Zhou et al., 2025b; Zhuang et al., 2024). Khayyaminejad et al. (2023) studied the influence of impeller's geometrical on performance, the finding shows pump head always increases with increasing blade length while a dual effect on efficiency is observed. The blade type also affect significantly on the circulating flow in casing. Front-bent blade exhibits better performance within vortex pump (Quan et al., 2021). In addition to ongoing effort to blade optimization, using winglets on the tip of the impeller blades have good effect on improving hydraulic performance (Machalski et al., 2021). The research work also presents optimal winglet placement on impeller blade. To state the influence of medium property on hydraulic performance, Rogovyi et al. (2021) and Li and Zhang (2018) conducted studies in pump performance both experimentally and numerically. The findings shows the medium viscosity has a less effect on both flow rate, but a significant influence on head and the efficiency of the pump that can be even reduced by 20% with increasing of plastic viscosity. Gao et al. (2021) optimized the vortex impeller by changing the key parameters including outer diameter outlet width of blades and blade angle at outlet, and investigated the inner flow field based on the optimal model. The results shows that backflow occurs at the pump entrance and the rotation direction is same with impeller. The backflow region moves along the pipe wall and latterly encounters with the approaching flow, which leads to vortex formation.

In the single-phase flow within the vortex pump, operating characters has attracted more attention. Li (2024) and Li (2025) studied the influence of wall roughness on operating performance. The results show that the fractional power and disk loss increases with increased wall roughness, which leads to that changing rates of predicted shaft-power are positive and the efficiency are negative for high wall roughness. Besides the effects of interface model in CFD simulation on vortex pump performance is also evaluated. Gerlach et al. (2017) conducted a comparison between Hamel-Oseen vortex and flow pattern with respect to the circumferential velocity, the vorticity and the axial velocity by simulation. The results shows that although the trajectories of the circumferential velocity within vortex pump were largely in line with the Hamel-Oseen vortex model, the vorticity presents opposite. Only at overload condition, the vorticity was in line with the predictions of the Hamel-Oseen vortex model. Chen et al. (2006) conducted a study on unsteady flow field within a vortex pump by numerical simulations. The work presents that the unsteady flow within the casing chamber affect the flow in the impeller and vice versa but has a relatively small effect on the unsteady flow in the impeller and in the hull. Quan et al. (2019b) investigated the performance and energy transition characters within a vortex pump. Based on the findings, it can be concluded that the demarcation between the circulating flow and other turbulent flow patterns is rather indistinct under low flow rate conditions. As the flow rate increases, the hydraulic losses stemming from it will become predominant in the front chamber. The main circulating flow vortex directly affects the pump's efficiency, whereas the subsidiary circulating flow vortices merely play an auxiliary role. As the flow rate approaches the design condition, the fluid within the pump tends to stabilize. During this process, the circulating flow vortices grow in size and assume regular shapes. Simultaneously, the geometric parameters of the main circulating flow vortex emerge as the crucial determinants of the pump's efficiency.

Currently, a great deal of research work has been carried out on vortex pumps. However, it mainly focuses on issues such as the optimization of impellers or other components, the influence of medium property on the operating performance, the wear characters in multi-phase flows, or the characteristics of vortex motion. The numerical studies of the unsteady fluctuation characters within vortex pumps are quite rare. Vortex pumps operate based on the dynamic interaction between a rotating impeller and fluid within an annular flow channel at high speed, creating a forced vortex motion in the fluid. Kinetic energy is repeatedly imparted to the fluid through successive blade passages, resulting in a cumulative pressure increase due to the regenerative transfer of energy. The fluid undergoes multiple helical recirculation along the flow path, amplifying its momentum before being expelled through the discharge port. This unique mechanism will lead to high-frequency pulsations of the flow parameters within the flow components and cause the impeller to naturally be subjected to alternating radial forces, which leads to problems such as vibration and noise, and has an impact on the fatigue life of the rotors.

This study presents a numerical analysis of a vortex pump, with respect to unsteady fluctuations and radial force acting on impeller. The distributions of pressure and velocity pulsations, as well as time-averaged pressure and velocity at the rotor-stator interface between the rotating and stationary components are meticulously presented. This is achieved by the technique of developing the revolved surface, which unfolds the impeller outlet and the inlet surfaces on both sides into a plane. Ultimately, a comprehensive evaluation of the radial forces exerted on the impeller is studied, offering critical insights into the mechanical loading characteristics of the rotating machinery component. These findings not only shed light on the complex unsteady flow mechanisms but also lay a solid groundwork for optimizing pump design and bolstering operational reliability.

2. NUMERICAL SIMULATION STATEGY

2.1 Pump Parameters and Mesh Generation

The model and numerical mesh division of the vortex pump is depicted in Fig. 1, accompanied by the test rig, impeller, and casing. The design parameters are demonstrated in Table 1. The number of blades on a single side of the impeller is 56, and the blades on the two sides are arranged in a staggered pattern as shown in Fig. 1.

(a) Text rig (b) Impeller (c) Casing

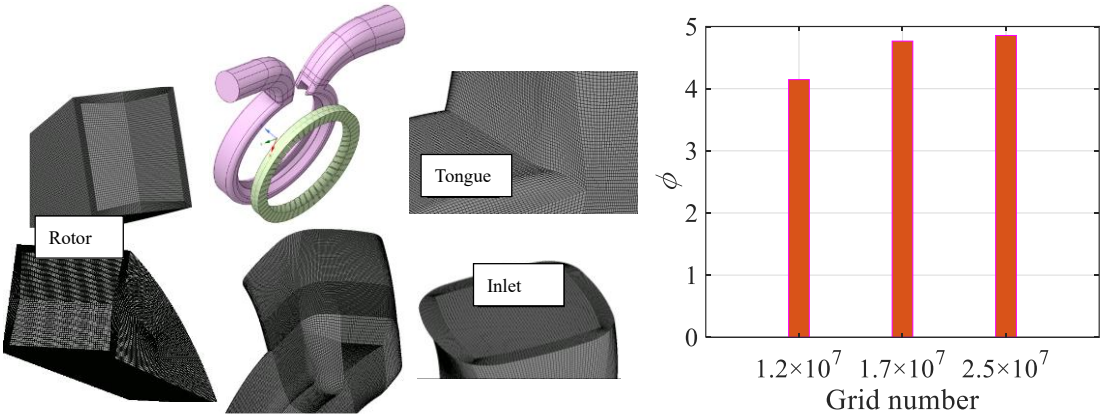

(d)Mesh generation (e) Grid convergence

Fig. 1 Mesh generation and grid convergence

Table 1 Design parameters of vortex pump

Design parameters	Value / unit
Flow rate/q	7.5 / m3/h
Rotation speed/n	2900 / rpm
Head/h	140 / m
Blade number on single side/z	56 / -

The computational domain of the vortex pump, includs the impeller, casing, and inlet/outlet pipe sections. Special attention was paid to regions with high flow gradients and complex geometries. The tongue region critical for flow interaction and performance, is meshed with refined elements to resolve complex flow patterns during blade passing. Seven-layer boundary layers with a growth rate of 1.1 were applied to all solid walls (impeller blades, casing wall, and inlet/outlet walls) to accurately capture viscous effects and boundary layer development.

The y+ value was maintained below 100 to ensure compatibility with the sst k-ω turbulence model. The axis direction clearance between the impeller tip and volute casing was discretized with several layers to resolve tip leakage flow. Grid convergence studies were performed by comparing head coefficients at the design flow rate (1.0 q_{des}) for coarse (1.2e7 elements), medium (2.7e7 elements), and fine (4.5e7 elements) meshes. The medium mesh which is adopt for present research showed less than 2% deviation from the fine mesh results as shown in the figure, confirming adequate resolution for subsequent simulations.

2.2 Numerical Setup and Experimental validation

The Shear Stress Transport (SST) k-ω turbulence model was employed to resolve the complex flow dynamics, as it accurately captures turbulence effects while retaining the robustness of the k-ε formulation. This approach has been extensively validated in centrifugal pump simulations (Zhu et al., 2025). The governing equations were solved using the commercial CFD software ANSYS CFX, with spatial discretization performed via the Finite Volume Method (FVM).

Following established methodologies for flow field analysis, the simulation time-step was calibrated to 0.0000574713 s, equivalent to a 1° angular displacement of the impeller. Boundary conditions included total pressure condition at the inlet and mass flow rate condition at outlet. All walls were treated as hydraulically smooth wall with no-slip constraints. A transient rotor-stator interface model was implemented to resolve time- dependent

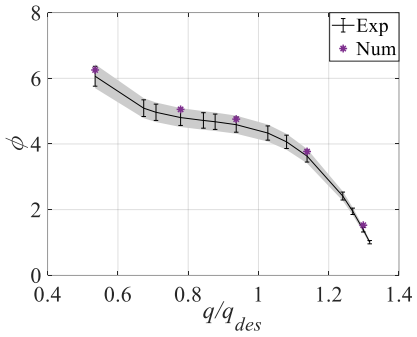

Fig. 2 Comparison between experimental and numerical head coefficient

rotor-stator interactions. Convergence was declared when normalized residuals dropped below 1×10-5 for all governing equations.

The unsteady simulation ran for more than 0.000574713 s, encompassing 10 complete impeller revolutions. Monitoring of flow variables confirmed the emergence of strictly periodic fluctuations after nine revolutions, ensuring steady initialization. Consequently, data from the final revolution were extracted for analysis and performance characterization.

Figure 2 illustrates the comparison between experimental and numerical head coefficient. It is clearly observed that the data points closely follow the trend of the experimental curve. At the design flow rate, the numerical head matches the experimental value with an error of 1.4%. Under off-design conditions, the maximum discrepancy is 5.2% at over load flow rate, well within acceptable engineering tolerances. The numerical simulation results are in good agreement with the experimental data, indicating that the numerical model can effectively capture the characteristics of the flow field, thus validating the reliability of the numerical simulation method employed in this study.

3. RESULTS AND DISCUSSION

Figure 3 demonstrates the frequency domain of pressure fluctuation at pressure probes. Six pressure probe points (P1 to P6) were strategically positioned to measure unsteady pressure fluctuations. P1 was set at the inlet pipe end (close to blade trailing edge). P2 was located at the outlet pipe start (close to blade trailing edge). P3 was set at the volute tongue. P4-P6 were set downstream of the tongue in the volute casing, evaluating pulsation attenuation and circumferential flow uniformity (P4: near impeller outlet; P5-P6: side walls of volute). C_p denotes the pressure coefficient, f represents the pressure fluctuation frequency, and f_s signifies the shaft frequency. It is observed that the shaft frequency dominates across all flow rate for the 6 probes.

The pressure spectrum of P1 and P2 exhibits distinct behaviors to other pressure probes. The dominant peak occurs at the impeller rotation frequency with prominent sub-synchronous components, indicating flow instability and recirculating vortices in the inlet and outlet pipes. These vortices form due to complex turbulence flow, causing periodic blockages and low-frequency pressure fluctuations. A distinct second harmonic, the blade passing frequency (56 f_s), is also prominent for all pressure probes, likely induced by helical flow with high outflow velocities from the impeller channels and vortices. These harmonics signify increased flow unsteadiness at the impeller discharge, which can excite structural vibrations for periodical radial force on impeller. The amplitude at dominant frequency for P1and P2 is clearly larger than that at other probes, nearly 40%-60% higher than that at locations far from the tongue (P4-P6) and 70% higher than P3. Besides, the amplitude reduces with flow rate increases.

The pressure spectrum of P3 exhibit further attenuation with a smallest amplitude among probes with 70% lower than at P2. Sub-synchronous components are nearly negligible. Since P2 and P3 are located at the start of the outlet pipe, periodic vortices exert a stronger effect in the downstream region due to the blocking effect of the wall where P2 is positioned. As the probe points away from tongue, P4-P6, sub-synchronous components of shaft frequency are negligible, confirms a uniform circumferential pressure distribution.

Figure 4 illustrates comparison between the amplitude of the pressure coefficient (C_p) at shaft frequency (f_s) and blade passing frequency (f_b) and the pressure pulsation intensity (C_{psdv}, quantified as the standard deviation of C_p) for six monitoring points (P1 to P6) at five flow rates, In order to more clearly observe the characteristics of pressure fluctuations at the key frequencies. The graph presents the same results as figure 3, indicating pronounced low-frequency fluctuations. It is illustrated that the shaft frequency is dominated across all flow rate for all probes. The blade passing frequency exhibit further attenuation indicating that the low frequency vortices are more stronger than high frequency ones. It can be seen from figure 4(f), P2 not only exhibits higher amplitude but also shows stronger pressure fluctuation intensity than other probes as the standard deviation is significantly bigger than other probes.

It is observed in figure (f) that the pressure pulsation reduces with flow rate decreasing. Though amplitude at shaft and blade passing frequency at P5 is lower than P1, the pressure pulsation is bigger than P1 at partial load condition. At partial load condition, the amplitude and fluctuation intense at P5 is higher than it at P4, indicating that the flow helix has stronger effect on that side which is clarified in the following content.

Figure 5 presents the circumferential distribution of pressure fluctuation intensity (C_{Psdv}) and time-averaged pressure coefficient (C_{pmean}) on the rotor-stator interface of a vortex pump across five flow rates. The interface comprises three key regions: OUT denotes the impeller outlet-stator inlet interface (corresponding to the volute tongue region), S1 is the right-hand interface from the inlet direction, and S2 is the left-hand interface from the inlet direction. The circumferential angle (θ_r) measured from the tongue tip and increases around the impeller rotation direction.

The time-averaged pressure increases from the inlet pipe to the outlet (θ_r changes from 0 to 330°). As flow rate

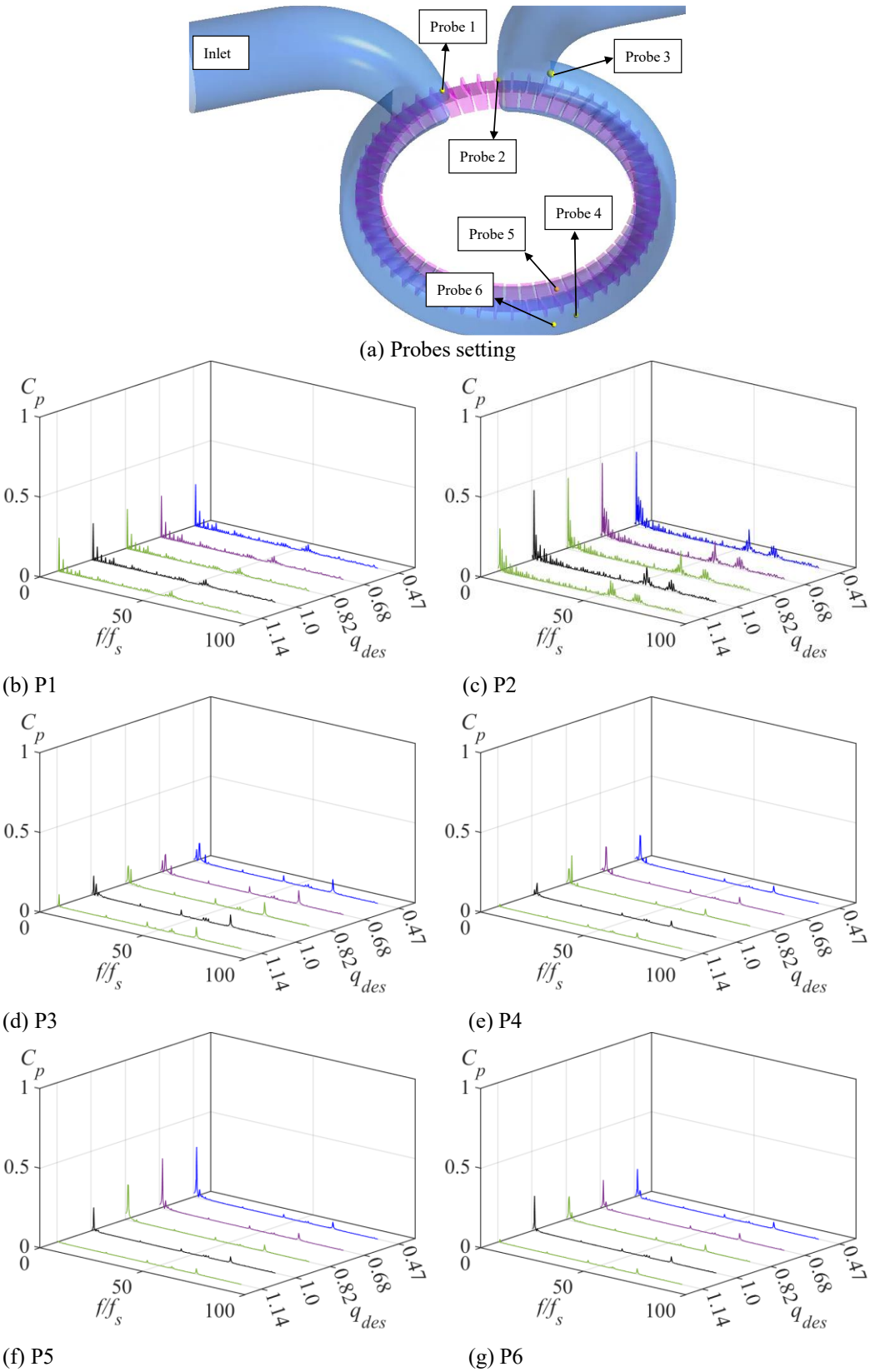

Fig. 3 Frequency domain of pressure fluctuation at pressure probes

increases, the time averaged pressure decreases. The pressure pulsation exhibits more pronounced as flow rate increasing. The distribution of pressure pulsation strength at impeller outlet presents relative symmetric. While the pressure pulsation at side interface exhibits stronger at the region close to impeller outlet as illustrated with rectangles. High-pressure pulsations at the impeller outlet occur in the regions adjacent to the side interfaces, as marked by circles. During the operation of a vortex pump, fluid continuously enters the impeller region from both lateral sides and exits the impeller outlet with helical vortices. These helical vortices significantly affect the flow field particularly in the region where the impeller inlet is adjacent to the outlet, leading to intensified pressure

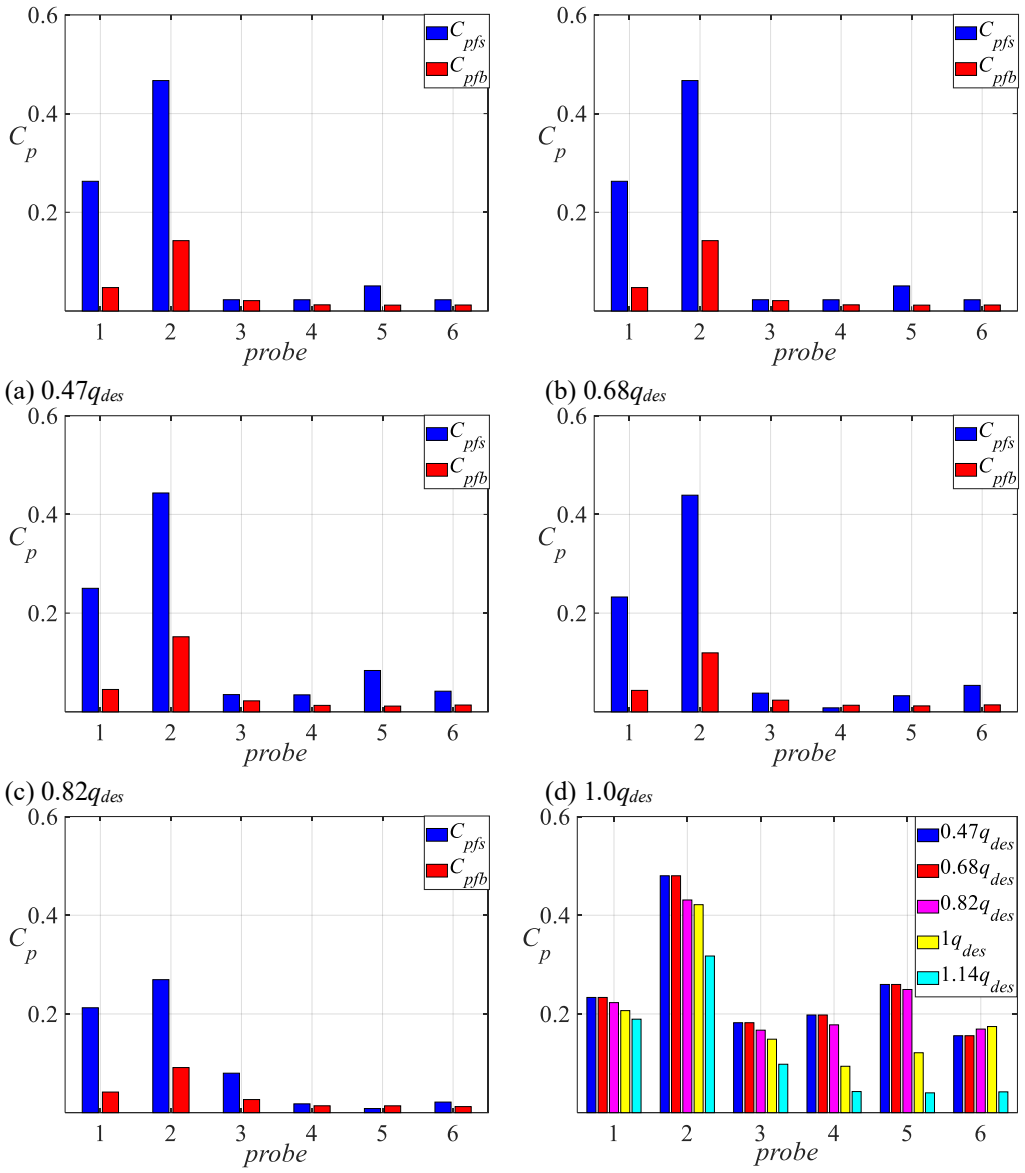

Fig. 4 Amplitude of C_p at shaft frequency and blade passing frequency and the standard deviation of C_p at different flow rate

and velocity fluctuations. Which contributes to the high-pressure pulsation in rectangles.

The low-pressure fluctuation zone is located within the region defined by $0<\theta_r<60$, marked with red rectangles that corresponds to the discharge end of the inlet pipe, forming a low-pressure region within the volute casing. As flow rate increases, the zone becomes bigger. At over load condition, the pressure pulsation at impeller outlet exhibits significantly smaller. When a vortex pump operates under over load conditions, the pressure should decreases. The fluid undergoes multiple recirculation between the impeller blades and the annular channel. During each revolution, the blades repeatedly accelerate the fluid, creating a helical vortex within the channel. This recirculation progressively amplifies the fluid's pressure and kinetic energy through successive interactions with the blades. Consequently, under high-flow regimes, the vorticity intensity and associated parameters diminish, thereby reducing the resultant pressure and velocity fluctuations.

Figure 6 shows the velocity fluctuation strength C_{vsdv} and mean value of C_v (velocity coefficient) as well as radial and circumferential velocity at rotor stator interface under partial and overload condition. At impeller outlet, regions with high velocity fluctuations exhibit obvious strip-shaped patterns as illustrated in Fig. (a), which correspond to the trailing edges of blades. As the impeller rotates, under the effect of fluid viscosity, the fluid at the blade trailing edge possess a higher circumferential velocity. Meanwhile, as fluid circulates repeatedly through the impeller vanes during the operation of the vortex pump, there is a relatively high jet flow intensity with high radial velocity at the blade outlets as displayed in Fig. (c). Coupled with the influence of the fluid helix, a relatively large intensity of velocity fluctuations exhibits in the fluid at the blade trailing edges.

The distributions of the regions with high velocity fluctuations on the two side interface are similar to the distribution of the pressure fluctuations, both being located on the side close to the impeller outlet as marked

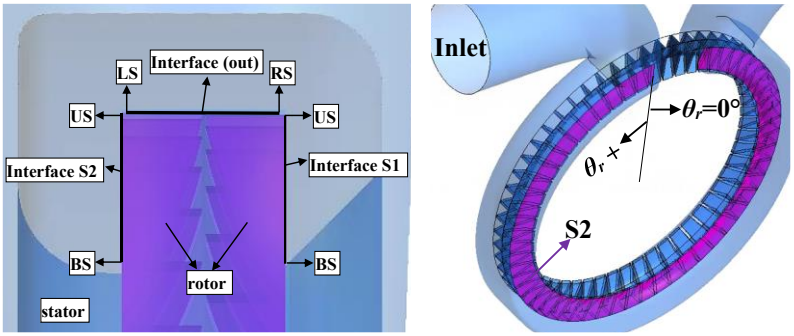

(a) Mornitor faces and parameters

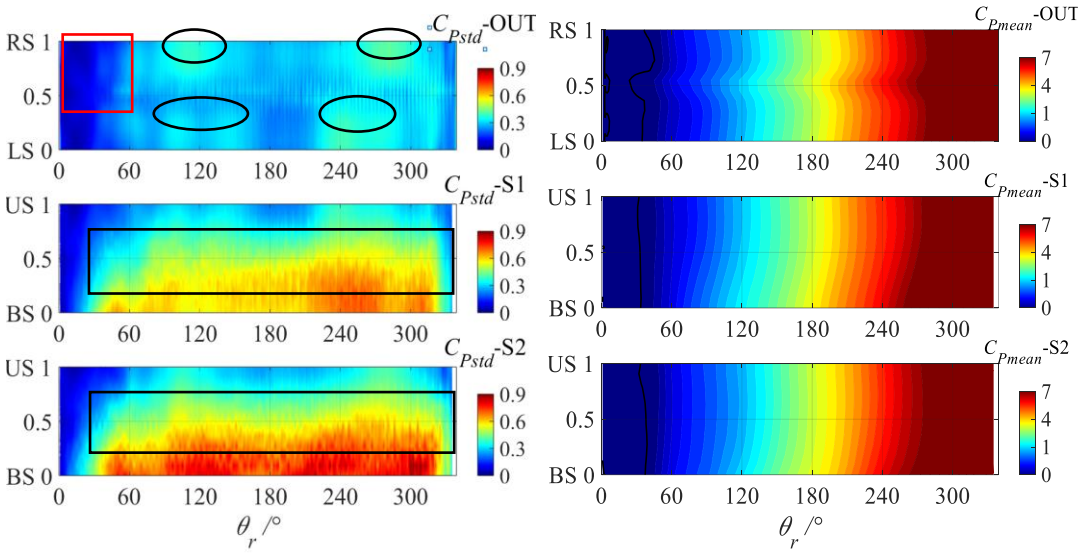

(b) $0.47q_{des}$

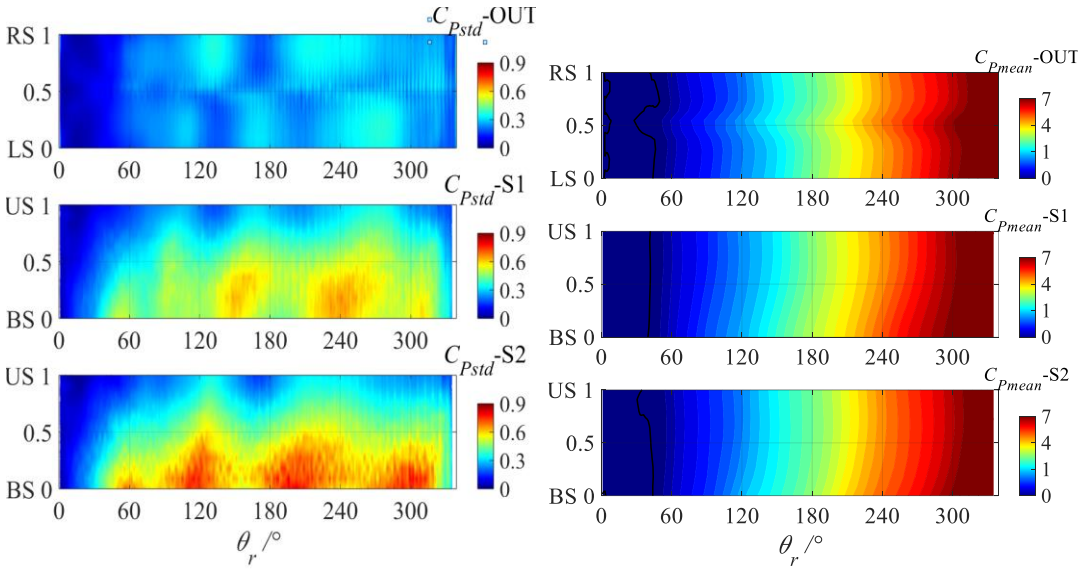

(c) $0.68q_{des}$

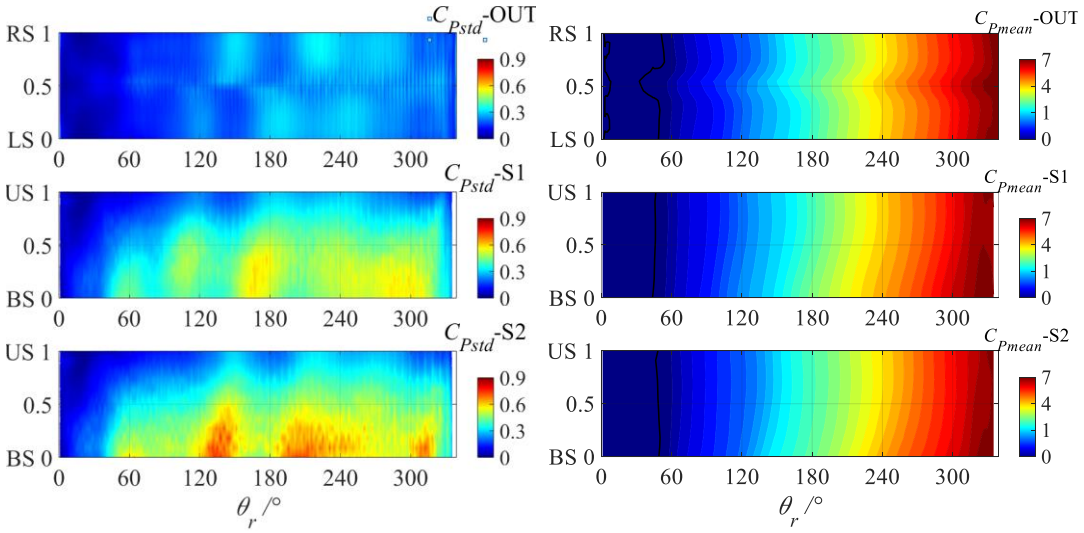

(d) $0.82q_{des}$

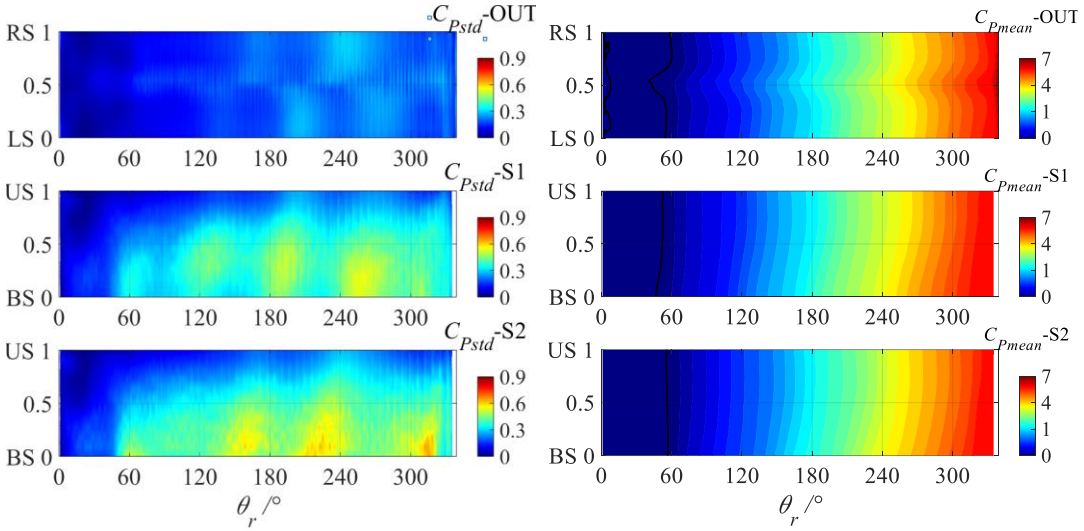

(e) $1.0q_{des}$

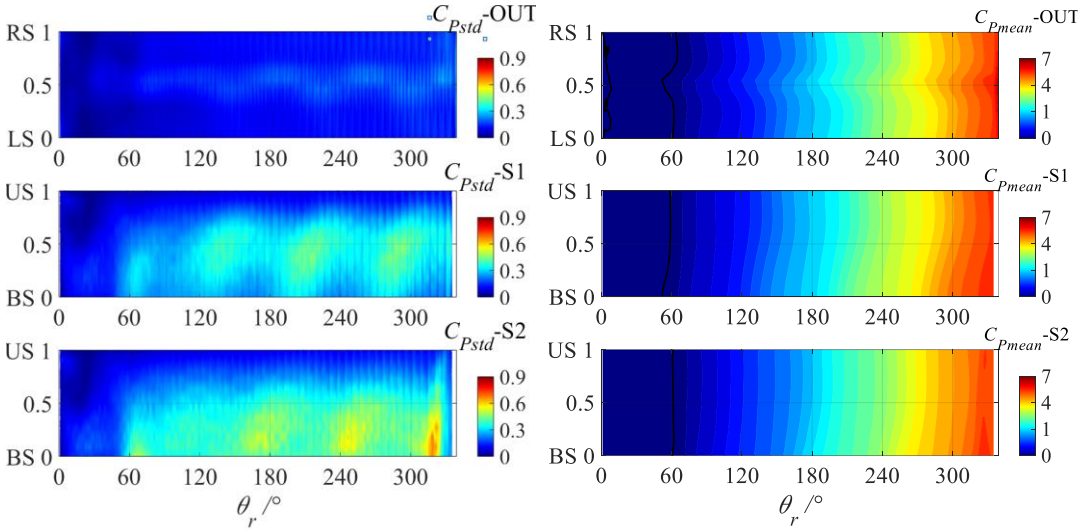

(f) $1.14q_{des}$

Fig. 5 Pressure fluctuation intensy C_{psdv} and mean value of C_p at rotor stator interface

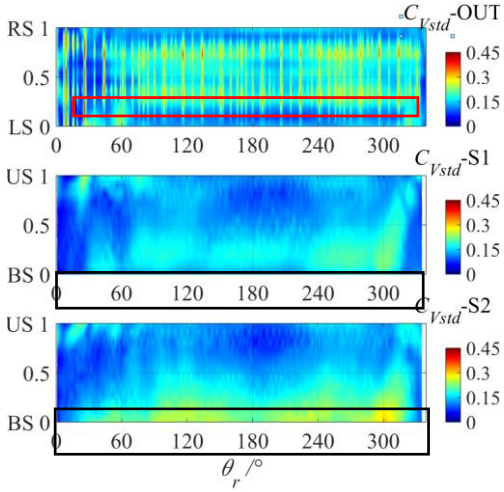

(a) Velocity fluctuation intense C_{vsdv} at $0.47q_{des}$

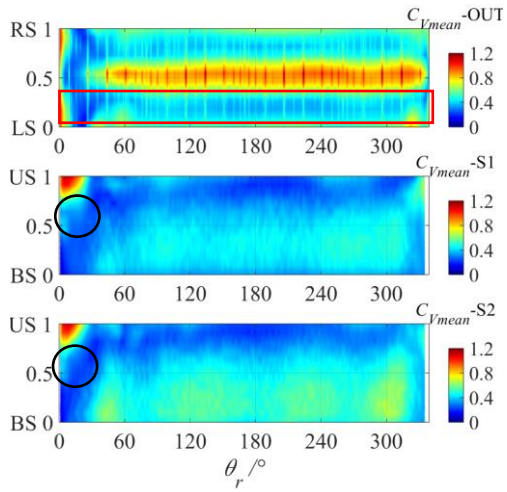

(b) Time averaged velocity C_{Vmean} at $0.47q_{des}$

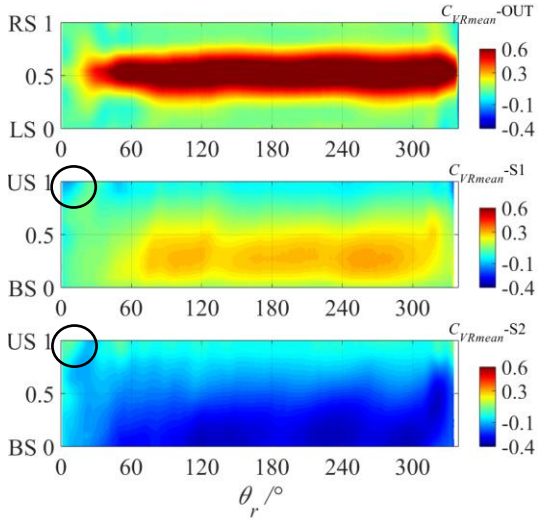

(c) Time averaged radial velocity V_R at $0.47q_{des}$

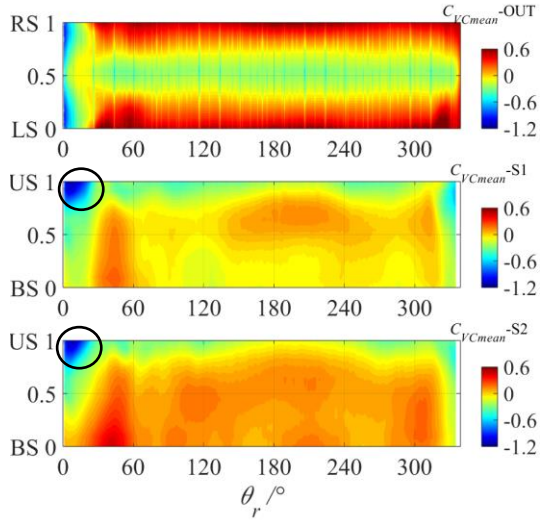

(d) Time averaged circumferential velocity V_C at $0.47q_{des}$

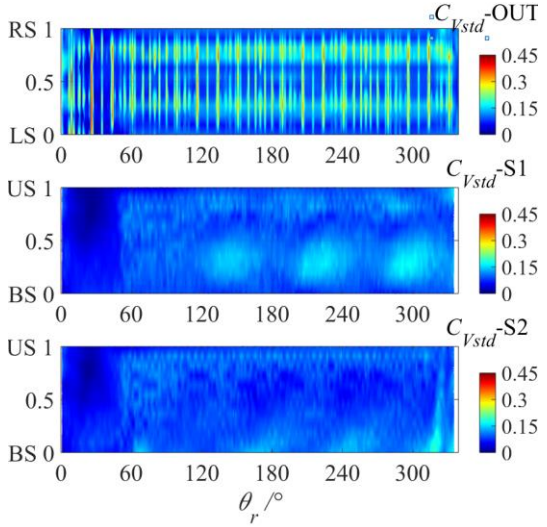

(e) Velocity fluctuation intense C_{vsdv} at $1.14q_{des}$

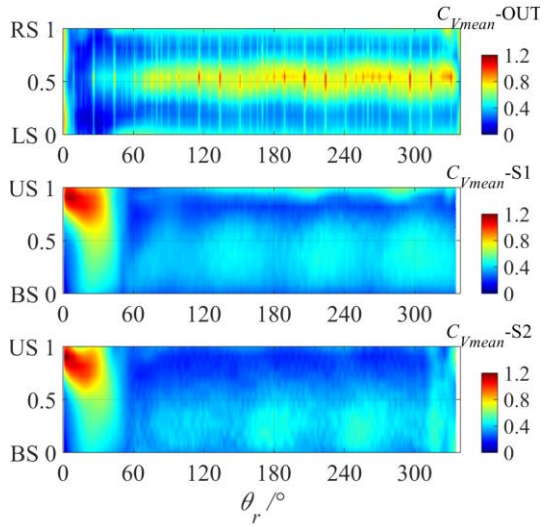

(f) Time averaged velocity C_{Vmean} at $1.14q_{des}$

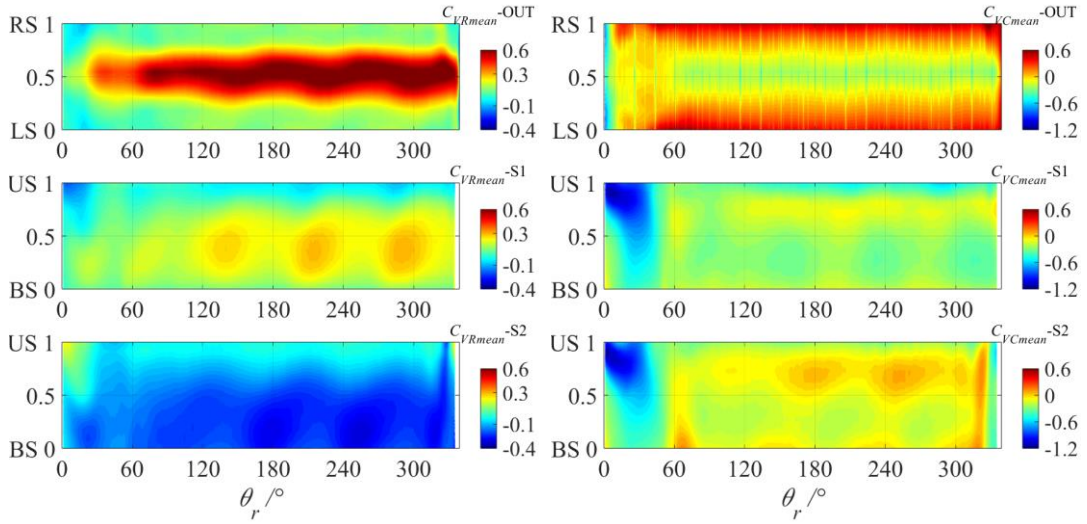

(g) Time averaged radial velocity V_R at $1.14q_{des}$ (h) Time averaged circumferential velocity V_C at $1.14q_{des}$

Fig. 6 Velocity fluctuation intense C_{vsdv} and mean value of C_V(velocity coefficient) at rotor stator interface

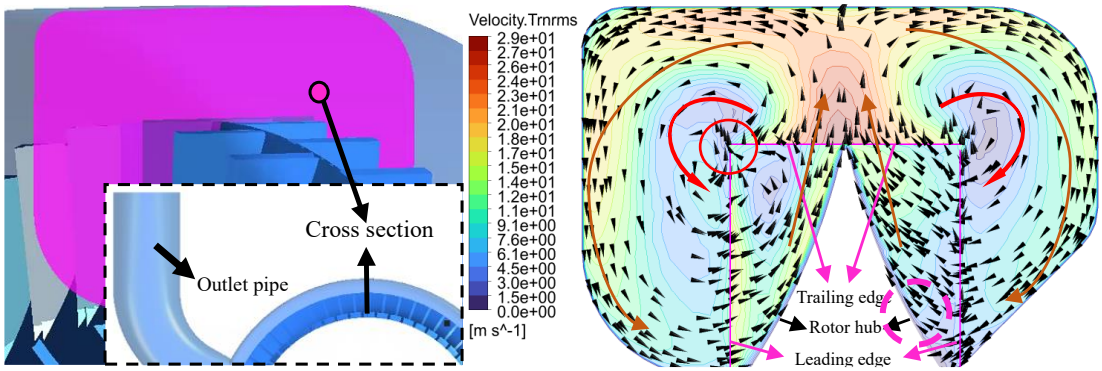

Fig. 7 Root mean square of velocity and time averaged velocity vector at cross section

with rectangles in Fig. (a). This side is more significantly influenced by the helical flow, leading to stronger velocity and pressure fluctuations.

It is demonstrated in Fig. (b), higher time-averaged velocity region at the impeller outlet appears in the middle area, as indicated by the red-marked region in the figure. This region is located at the blade partition of the impeller, where the fluid has a higher radial velocity as illustrated in Fig. (c). It should be noted that the velocity fluctuations in the marked region with lower velocity fluctuation than those in the adjacent regions on both sides. A local high-velocity region appears at the interface on two sides as marked in Fig. (b) with circles. This should be attributed to that after the impeller passages rotate past the tongue of the casing and enter the inlet region, the high-pressure fluid inside rapidly flows out from the outlet of the passages, and the fluid flows in from the bottoms of the two sides of the impeller, resulting in a relatively high radial velocity. Moreover, when the fluid enters the impeller inlet region from the inlet pipe, a high-speed recirculation zone appears on the side of the interface, leading to a relatively large circumferential velocity as illustrated with circles in Fig. (c) and (d). As flow rate increases, the velocity fluctuation and time averaged velocity exhibits attenuation however the mean value of radial and circumferential velocity increases.

Figure 7 shows the distribution of velocity root mean square (RMS) and time-averaged velocity vectors at a cross-section. As vortex pump operates, helical vortex within the fluid forms, enabling energy transfer through repeated interactions between the impeller and the fluid. The helical vortex results in a toroidal vortex in the section as shown in Fig. 7, inducing a spiral flow path in the peripheral channel. Two counter-rotating circumferential vortices are observed at the cross section as marked by red arrows, inducing significantly higher velocities on the impeller hub side. This results in a notably greater radial velocity near the hub side at the impeller outlet compared to other zones. Additionally, a similarly high velocity is induced along the volute outer near wall region as shown with brown arrows. As fluid circulates repeatedly through the impeller vanes during the operation of the vortex pump, the pressure, velocity in the affected-region should exhibits more intensive fluctuations.

In regions adjacent to the vortex core, the vortex-induced velocities are relatively low, accompanied by diminished intensity of velocity and pressure fluctuations. However, within the area marked by the red circle in the figure, the outer blade tip the impeller at the junction of the leading and trailing edges, elevated velocity and pressure fluctuations are observed. This phenomenon arises due to the proximity of this region to the impeller's

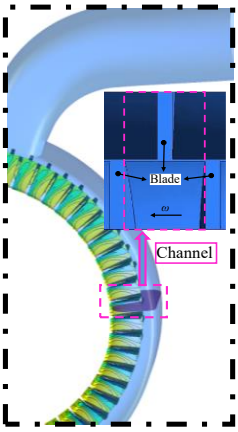

(a) Channel location

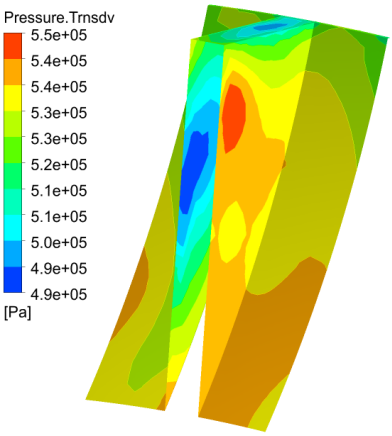

(b) C_{psdv} at upper channel wall at $0.47q_{des}$

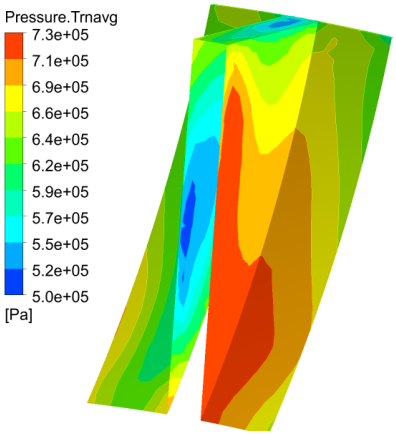

(c) Time averaged C_p at upper channel wall at $0.47q_{des}$

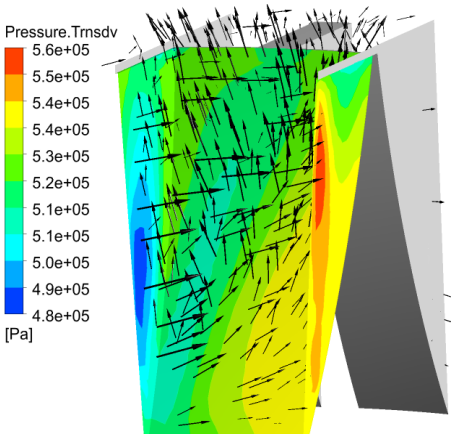

(d) C_{psdv} at lower channel wall at $1.14q_{des}$

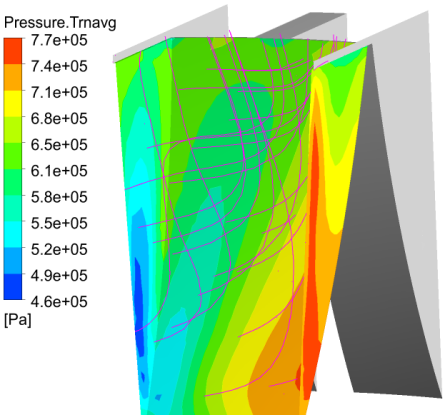

(e) Time averaged C_p at lower channel wall at $1.14q_{des}$

Fig. 8 Pressure fluctuation and stream line in a impeller channel at $0.47q_{des}$ and$1.14q_{des}$

geometric discontinuity. As the impeller rotates at high speed, the intensified blade tip wake effects dominate here, leading to stronger velocity and pressure fluctuations compared to other regions.

Besides, the cross-sectional shapes of the volutes on the two sides of the impeller are different as shown with the dotted circle. In this region, due to the requirements of the overall machine design, the change of its boundary is not gradual, which results in a large curvature of the flow in this region, leading to relatively large velocity and pressure fluctuations as illustrated in Fig. 4.

Figure 8 shows time averaged pressure and fluctuation intense on rotor and velocity vector in side channel. Two single flow passages (the upper and lower ones shown in Fig. (a)), corresponding to the cross-section highlighted in Fig. 7, are selected for analysis

The time-averaged pressure and pressure fluctuation distributions exhibit minor discrepancies between the upper and lower channels but follow analogous trends. This behavior is primarily attributable to divergent inflow conditions induced by asymmetries in the volute cross-sectional geometry on the impeller sides.

Elevated pressure fluctuation intensity appears in two distinct regions: the blade pressure side and the hub root region adjacent to the pressure surface. In contrast, the blade suction side and remaining hub regions exhibit significantly lower pressure fluctuation intensity. Simultaneously, the time-averaged pressure distribution demonstrates a spatial pattern analogous to that of the pressure fluctuation intensity.

Due to the high-speed rotation of the impeller, as the fluid enters the dual blade passages from both inlets, the primary flow exhibits an incidence angle, impinging on the pressure surface of the blades. Conversely, flow separation on the blade suction side induces vortices. Concurrently, streamline patterns reveal a helical flow motion, ultimately resulting in elevated pressure fluctuations and time-averaged pressure magnitudes on the pressure surface, whereas the suction surface exhibits comparatively weaker pressure fluctuations.

Figure 9 demonstrates the radial force acting on impeller during one impeller rotation under different flow rate and force vector at $0.47q_{des}$ for one impeller revolution. In vortex pumps, fluid energy is progressively augmented through continuous interactions with impeller blades, leading to a gradual pressure rise from the inlet to the outlet. Consequently, the impeller inevitably experiences significant radial forces due to this pressure gradient as shown in the figure. The resultant magnitude of radial forces oscillates synchronously with impeller rotation due to periodic pressure fluctuations. As

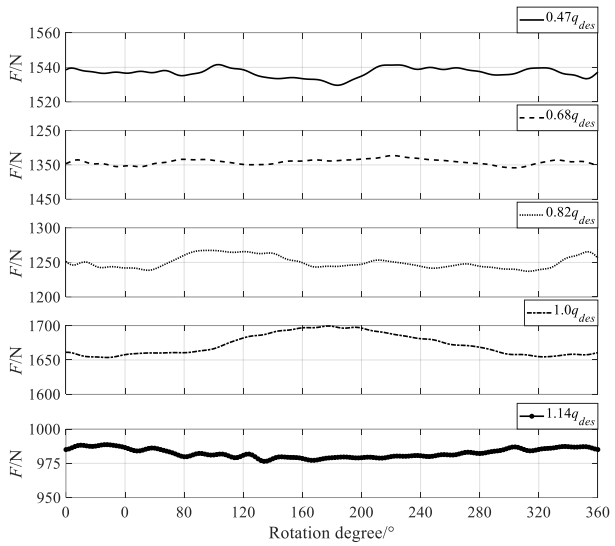

(a) Radial force under different flow rate

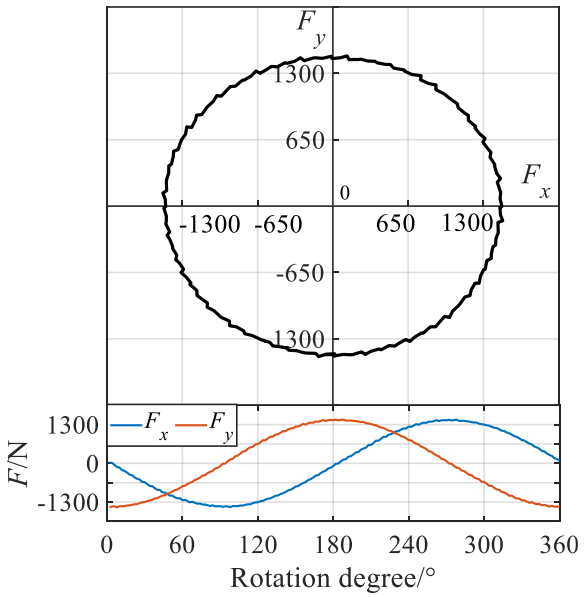

(b) Force vector at 0.47q_{des}

Fig. 9 Radial force acting on the impeller during one impeller rotation

illustrated in the Fig. (a), the amplitude of these resultant force oscillations remains relatively low.

As evident from Fig. (b), the radial force components acting on the impeller exhibit well-defined periodic oscillations synchronized with the impeller rotation, alternating between positive and negative values. This indicates that while the magnitude of the radial forces remains relatively stable during rotation, their direction undergoes continuous reversal. The observed behavior implies that under high-speed operation, the impeller is subjected to substantial alternating stresses. These cyclic loads can significantly affect the fatigue strength of the shaft, necessitating careful consideration in design and analysis.

4. CONCLUSION

This study presents a comprehensive investigation into unsteady fluctuations in a vortex pump. Pressure pulsations at typical locations are examined, along with the distributions of pressure/velocity fluctuation intensities and time-averaged values at the rotor-stator interface. The causes of pressure and velocity pulsation patterns are revealed. Finally, the transient radial force acting on the impeller is studied. The following conclusions were drawn:

(1) The pressure pulsations are dominated by the shaft frequency even in regions far from the casing tongue, and the effect of the blade frequency is much smaller than that of the shaft frequency. This differs significantly from vane pumps. The pressure pulsation amplitude at the tongue monitoring point(P2) is the highest, nearly 40% - 60% higher than that at locations far from the tongue(P4-P6) and 70% higher than that upstream of the outlet pipe(P3).

(2) The pressure pulsation intensity at the impeller outlet is higher in the side areas than in the middle area. At the inlets on both sides of the impeller, the pressure pulsation intensity in the area near the outlet is significantly greater than that in other areas. The distribution of velocity pulsation at the inlets on both sides of the impeller is similar to that of pressure pulsation. Both are affected by the fluid helix at the outlet and exhibit relatively large values.

(3) The pressure acting on the impeller mainly originates from the pressure surface of the blades and the area of the hub close to the pressure surface. The main flow has presents attack angle that deflects towards the pressure surface, resulting in a relatively large pressure in the hub area. The pressure in the area of the back surface is relatively small due to the influence of flow separation. The direction of the radial force acting on the impeller changes periodically with impeller rotation at the shaft frequency.

ACKNOWLEDGEMENTS

The authors disclosed receipt of the following financial support for the research, authorship, and/or publication of this article: This study is supported by the Science and Technology Support Program of Taizhou City (No. TG202320). The supports are gratefully acknowledged. Dr. Waqar Ahmed Qureshi1 is gratefully acknowledged for professionally polishing the language of this paper, which has significantly enhanced its readability and academic presentation.

CONFLICT OF INTEREST

We declare that we do not have any commercial or associative interest that represents a conflict of interest in connection with the work submitted.

AUTHORS CONTRIBUTION

Yangyang Wei: Funding acquisition, Investigation; **Hongliang Wei:** Writing – original draft, Formal analysis; **Quanwang Fan:** Data curation; **Xiuli Wang:** Software, Writing – review & editing.

REFERENCES

Červinka, M. (2012). Computational study of sludge pump design with vortex impeller. *Engineering Mechanics*, *87*.

Chen, H. X., Shi, F. J., & Guo, J. (2006). Numerical research on the three dimensional unsteady flow within the vortex pump. *International Journal of Turbo and Jet Engines*, *23*(1), 27-36.

Gao, X., Shi, W., Zhao, R., Zhao, T., & Wang, H. (2021). Optimization design and internal flow field study of open-design vortex pump. *Shock and Vibration*, *2021*(1), 6673200. https://doi.org/10.1155/2021/6673200

Gerlach, A., Preuss, E., Thamsen, P. U., & Lykholt-Ustrup, F. (2017). Numerical simulations of the internal flow pattern of a vortex pump compared to the Hamel-Oseen vortex. *Journal of Mechanical Science and Technology*, *31*, 1711-1719. https://doi.org/10.1515/TJJ.2006.23.1.27

He, D. H., Wang, G., Liu, Z., & Huang, R. (2023). Bubble breakage and aggregation characteristics in a vortex pump under bubble inflow. *Physics of Fluids*, *35*(9). https://doi.org/10.1063/5.0168639

Imasaka, Y., Kanno, H., Saito, S., Miyagawa, K., Nohmi, M., Isono, M., & Kawai, M. (2018). Clogging mechanisms of vortex pumps: Fibrous material motion capture and simulation with a CFD and DEM coupling method. *Fluids Engineering Division Summer Meeting*, https://doi.org/10.1115/FEDSM2018-83503

Khayyaminejad, A., Khabazi, N. P., Gholami-Malek Abad, F., & Taheripour, S. (2023). Numerical investigation on the effect of the geometric parameters of the impeller on vortex pump performance. *Iranian Journal of Science and Technology, Transactions of Mechanical Engineering*, *47*(4), 1711-1731. https://doi.org/10.1007/s40997-023-00639-9

Li, W. (2024). Effects of interface model on performance of a vortex pump in CFD simulations. *International Journal of Fluid Engineering*, *1*(1). https://doi.org/10.1063/5.0196213

Li, W. (2025). Performance of vortex pump in CFD simulations with rough walls. *International Journal of Fluid Engineering*, *2*(1). https://doi.org/10.1063/5.0237732

Li, W., & Zhang, Y. (2018). The vortex pump under highly viscous liquid flow conditions. *Arabian Journal for Science and Engineering*, *43*, 4739-4761. https://doi.org/10.1007/s13369-018-3112-7

Machalski, A., Skrzypacz, J., Szulc, P., & Błoński, D. (2021). Experimental and numerical research on influence of winglets arrangement on vortex pump performance. *Journal of Physics: Conference Series*, https://doi.org/10.1088/1742-6596/1741/1/012019

Mohsin, A. T., & Yaqob, B. N. (2022). Experimental investigation on improving lifetime of peripheral pump impeller under cavitation using different techniques. *International Journal of Heat & Technology*, *40*(5). https://doi.org/10.18280/ijht.400518

Quan, H., Chai, Y., Li, R., & Guo, J. (2019a). Numerical simulation and experiment for study on internal flow pattern of vortex pump. *Engineering Computations*, *36*(5), 1579-1596. https://doi.org/10.1108/EC-09-2018-0420

Quan, H., Chai, Y., Li, R., Peng, G. Y., & Guo, Y. (2019b). Influence of circulating-flow's geometric characters on energy transition of a vortex pump. *Engineering Computations*, *36*(9), 3122-3137. https://doi.org/10.1108/EC-03-2019-0082

Quan, H., Li, Y., Kang, L., Yu, X., Song, K., & Wu, Y. (2021). Influence of blade type on the flow structure of a vortex pump for solid-liquid two-phase flow. *Machines*, *9*(12), 353. https://doi.org/10.3390/machines9120353

Rogovyi, A., Korohodskyi, V., Khovanskyi, S., Hrechka, I., & Medvediev, Y. (2021). Optimal design of vortex chamber pump. *Journal of Physics: Conference Series*, https://doi.org/10.1088/1742-6596/1741/1/012018

Yang, W., Zhang, R., Wang, X., & Guo, G. (2025). Cavitation-induced variations in vortex structure and energy conversion dynamics in a vortex pump. *Energy*, *317*, 134478. https://doi.org/10.1016/j.energy.2025.134478

Ye, D., Li, H., Ma, Q., Han, Q., & Sun, X. (2020). Numerical investigation of performance improvement and erosion characteristics of vortex pump using particle model. *Shock and Vibration*, *2020*(1), 5103261. https://doi.org/10.1155/2020/5103261

Zeng, W., Zhou, P., Wu, Y., Wu, D., & Xu, M. (2024). Multi-cavitation states diagnosis of the vortex pump using a combined DT-CWT-VMD and BO-LW-KNN based on motor current signals. *IEEE Sensors Journal*. https://doi.org/10.1109/JSEN.2024.3446170

Zhang, D., Yang, M., Gao, B., & Lu, B. (2013). Particle concentration distribution and its effect on performance in a vortex pump. *Fluid Machinery*, *41*(5), 15-18.

Zhou, P., Li, J., Wu, Y., Wang, Y., Zhou, X., Wen, Z., & Zhao, H. (2025a). Study of cavitation-induced flow characteristics of a vortex pump based on coherence analysis. *Physics of Fluids*, *37*(3). https://doi.org/10.1063/5.0254026

Zhou, P., Wen, Z., Wang, Y., Wu, Y., Wu, D., Huang, R., &

Yao, Z. (2025b). Improving the energy performance of vortex pump based on whale optimization algorithm. *Engineering Applications of Computational Fluid Mechanics*, *19*(1), 2441344. https://doi.org/10.1080/19942060.2024.2441344

Zhu, X., Han, X., Xie, C., Zhang, H., & Jiang, E. (2025). Numerical investigation of clocking effect on fluctuating characters and radial force within impeller for a centrifugal pump. *Journal of Applied Fluid Mechanics*, *18*(3), 549-566. https://doi.org/10.47176/jafm.18.3.2843

Zhuang, H., Liu, M., & Cao, L. (2024). Design and performance prediction of a vortex pump based on CFD for high concentration sludge dredging. *Journal of Physics: Conference Series*, https://doi.org/10.1088/1742-6596/2752/1/012111